



# Photocatalytic activity of ZnO/Sn<sub>1-x</sub>Zn<sub>x</sub>O<sub>2-x</sub> nanocatalysts: A synergistic effect of doping and heterojunction



Lirong Zheng<sup>a,1</sup>, Chongqi Chen<sup>a,1</sup>, Yuanhui Zheng<sup>b,\*</sup>, Yingying Zhan<sup>a</sup>, Yanning Cao<sup>a</sup>,  
Xingyi Lin<sup>a</sup>, Qi Zheng<sup>a,\*\*</sup>, Kemei Wei<sup>a</sup>, Jiefang Zhu<sup>c,\*\*\*</sup>

<sup>a</sup> National Engineering Research Center of Chemical Fertilizer Catalyst, Fuzhou University, Gongye Road 523, Fuzhou 350002, Fujian, China

<sup>b</sup> Division of Materials Science and Engineering, Commonwealth Scientific and Industrial Research Organization, Clayton South, Victoria 3169, Australia

<sup>c</sup> Department of Chemistry – Angstrom Laboratory, Uppsala University, Uppsala 75121, Sweden

## ARTICLE INFO

### Article history:

Received 28 June 2013

Received in revised form 18 October 2013

Accepted 21 October 2013

Available online 28 October 2013

### Keywords:

SnO<sub>2</sub>

ZnO

Doping

Heterojunction

Photocatalysis

## ABSTRACT

A novel configuration of porous ZnO/Sn<sub>1-x</sub>Zn<sub>x</sub>O<sub>2-x</sub> heterojunction nanocatalyst with high photocatalytic activity was successfully synthesized through a simple two-step solvothermal method. Porous Sn<sub>1-x</sub>Zn<sub>x</sub>O<sub>2-x</sub> was synthesized from Zn<sup>2+</sup> and Sn<sup>4+</sup> precursors with the Zn/Sn ratio of 2:1 in the absence of alkali, and then intermolecular dehydrolysis led to the formation of heterointerface between Sn<sub>1-x</sub>Zn<sub>x</sub>O<sub>2-x</sub> and ZnO. The results show that Zn<sup>2+</sup> doping exhibits a significant influence on particle size of SnO<sub>2</sub> leading to much higher specific surface area and larger band gap, which is in favor of the photocatalytic activity of SnO<sub>2</sub> under UV light irradiation. In addition, the formation of ZnO/Sn<sub>1-x</sub>Zn<sub>x</sub>O<sub>2-x</sub> heterostructure improves the separation of photogenerated electron–hole pairs due to the potential difference between Sn<sub>1-x</sub>Zn<sub>x</sub>O<sub>2-x</sub> and ZnO, which also benefits to photocatalysis. By taking account of them together, these results provide further insight into the synergistic effects of metal ion doping and semiconductor/semiconductor heterostructure on the activity of photocatalysts in environmental remediation applications.

© 2013 Elsevier B.V. All rights reserved.

## 1. Introduction

Photocatalytic treatment of wastewater by irradiated semiconductor has proven to be an effective process, which can lead to complete mineralization of pollutants [1]. Moreover, semiconductor photocatalysts have been widely employed in production of hydrogen by splitting water [2–6], purification of air [7], and other applications [8]. However, the fast recombination of the photo-generated electrons and holes hinders the commercialization of this technology. Therefore, it is important to promote photocatalytic efficiency by suppressing the recombination [9]. Previous studies indicated that photocatalytic activity largely depends on two factors: reactant adsorption behavior and the separation efficiency of electron–hole pairs [10]. The adsorption capacity can be improved by increasing the specific surface area of the catalysts, while semiconductor modifications by doping with transitional

metal ion [11–13], coupling with another semiconductor [14–17], and loading with noble metals [18–24] have been successfully carried out, in order to reduce the recombination of the electrons and holes.

ZnO and SnO<sub>2</sub> are wide direct bandgap semiconductors and considered as promising functional materials due to their highly gas-sensitive and excellent optical properties. Recently, it has been proved that composite materials of ZnO and SnO<sub>2</sub> with a heterojunction structure showed superior physical and chemical properties to their individual materials [25]. For example, previous research on network ZnO/SnO<sub>2</sub> nanocatalysts indicates that the SnO<sub>2</sub>–ZnO heterojunction can improve the separation of photogenerated electron–hole pairs and exhibits higher photocatalytic activity than pure SnO<sub>2</sub> and ZnO [26–29]. In addition, it was recently found that Zn doping has a promoting effect on photocatalytic activity of SnO<sub>2</sub> [30–32]. Until now, only one kind of SnO<sub>2</sub> modifications mentioned above has been discussed in each published literature. In this work, we introduce a novel photocatalyst of ZnO/Sn<sub>1-x</sub>Zn<sub>x</sub>O<sub>2-x</sub>, and intend to enhance the photocatalytic activity via the synergistic effects from metal ion doping and heterostructure.

To the best of our knowledge, there is no report about studying the synergistic effect of heterojunction and doping on photocatalytic performance of metal oxides. In this work, we prepared novel

\* Corresponding author. Tel.: +61 3 99024078; fax: +61 3 99024078.

\*\* Corresponding author. Tel.: +86 591 8373 1234 8112; fax: +86 591 8373 8808.

\*\*\* Corresponding author. Tel.: +46 18 471 3722; fax: +46 18 51 3548.

E-mail addresses: [yuanhui.zheng@csiro.au](mailto:yuanhui.zheng@csiro.au) (Y. Zheng), [zhengqi@fzu.edu.cn](mailto:zhengqi@fzu.edu.cn)

(Q. Zheng), [jiefang.zhu@kemi.uu.se](mailto:jiefang.zhu@kemi.uu.se) (J. Zhu).

<sup>1</sup> Both authors contributed equally to this work.

ZnO/Sn<sub>1-x</sub>Zn<sub>x</sub>O<sub>2-x</sub> photocatalysts by a two-step solvothermal method. In the first step, only Zn doped SnO<sub>2</sub> (described as Sn<sub>1-x</sub>Zn<sub>x</sub>O<sub>2-x</sub>) was formed via hydrolyzation at low pH condition. In the next step, NaOH was added to react with residual Zn precursor, leading to the formation ZnO/Sn<sub>1-x</sub>Zn<sub>x</sub>O<sub>2-x</sub> heterostructured nanocatalysts. The roles of metal-ion doping and heterostructure on photocatalytic activity were systematically investigated. It was found that both Zn doping and heterostructure promote the formation of hydroxyl radicals ( $\bullet$ OH) on the surface of ZnO/Sn<sub>1-x</sub>Zn<sub>x</sub>O<sub>2-x</sub> photocatalysts under UV illumination, thus enhancing photocatalytic activity.

## 2. Experimental

### 2.1. Chemicals and synthesis

Zinc acetate, tin tetrachloride, sodium hydroxide, coumarin and ethanol were of analytical grade and purchased from Sinopharm Chemical Reagent Co., Ltd. without further purification.

ZnO/Sn<sub>1-x</sub>Zn<sub>x</sub>O<sub>2-x</sub> was synthesized by a two-step solvothermal process. 2 mmol of Zn(OAc)<sub>2</sub>·2H<sub>2</sub>O and 1 mmol of SnCl<sub>4</sub>·5H<sub>2</sub>O were added to 30 mL of ethanol to form a suspension. After being vigorously stirred for 30 min, both precursors were dissolved at room temperature. The solution was transferred to 50 mL Teflon-lined stainless steel autoclave, and kept at 160 °C for 24 h. The pH value was measured with a pH meter (RPB 10, Shanghai Hengci Electronic Technology Co., Ltd.) before and after reaction. After the reaction, 2n mL of 0.5 M NaOH ethanol solution (for samples B, C, and D: n = 0, 1, and 2, respectively) and (10–2n) mL ethanol were added into the autoclave with stirring (i.e. the total volume of added solution is 10 mL). The sealed autoclave was put into an oven again, and kept at 160 °C for another 16 h. For comparison, pure ZnO and SnO<sub>2</sub> were also synthesized by a solvothermal method: 30 mL of 0.1 M Zn(OAc)<sub>2</sub> or 0.1 M SnCl<sub>4</sub> ethanol solution was poured into a Teflon-lined stainless steel autoclave with a capacity of 50 mL. The sealed reactor was heated to 160 °C, and maintained at this temperature for 24 h. The final products were collected by centrifugation, washed with deionized water and ethanol for several times, and finally dried in the air at 80 °C for 10 h.

### 2.2. Characterization

The powder X-ray diffraction (XRD) patterns of the samples were recorded by a PANalytical X' Pert Pro diffractometer with Co K $\alpha$  radiation ( $\lambda$  = 0.179 nm) at a scanning rate of 0.12°/min. X-ray fluorescence (XRF) measurements were performed on a PANalytical Axios X-ray fluorescence spectrometer. N<sub>2</sub> adsorption/desorption measurements were carried out at 77 K using a Micrometrics ASAP 2020 system after the samples were degassed at 80 °C in a vacuum for 10 h. UV–vis diffuse-reflectance spectra (DRS) of the as-synthesized samples were obtained using a UV–vis–NIR spectrometer (Lambda 900). Fourier transform infrared spectra (FTIR) were obtained on a Perkin-Elmer IR spectrophotometer. Raman spectra were recorded with a Renishaw InVia micro-Raman spectrometer, coupled with a Leica microscope and equipped with a Peltier cooled CCD detector. Excitation was provided by a laser with the wavelength of 785 nm and power of 30 mW. Samples were scanned using a synchroscan mode from 100 cm<sup>-1</sup> to 3200 cm<sup>-1</sup>, and the acquisition time for each scan was 10 s. The X-ray photoelectron spectroscopy (XPS) measurements were performed on a Phi Quantum 2000 spectrophotometer with Al KR radiation (1486.6 eV). The resulting binding energies are calibrated by using that of C 1s (284.8 eV).

### 2.3. Analysis of hydroxyl radicals ( $\bullet$ OH)

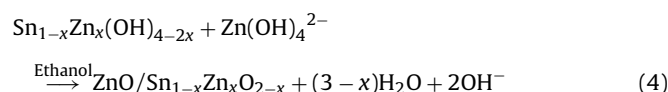
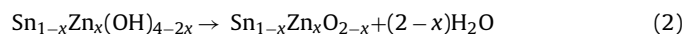
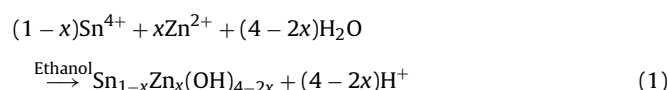
The analysis principle is that coumarin can readily react with  $\bullet$ OH radicals to produce highly fluorescent product, 7-hydroxycoumarin, which emits photoluminescence around 460 nm under the excitation with the wavelength of 332 nm. The intensity of the peak attributed to 7-hydroxycoumarin is proportional to the amount of  $\bullet$ OH radicals formed. Therefore, this photoluminescence technique using coumarin as a probe molecule has been used to detect the generation of  $\bullet$ OH [33]. An aqueous solution of  $1 \times 10^{-3}$  M coumarin was prepared. 10 mg of catalyst was added to 100 mL of  $1 \times 10^{-3}$  M coumarin solution in a 200 mL Pyrex glass vessel. At 5 min intervals, 5 mL aliquots were sampled, and centrifuged to remove the catalysts. The photoluminescence intensity of 7-hydroxycoumarin was tracked by a HITACHI F-4600 fluorescence spectrophotometer.

### 2.4. Photocatalytic performance measurements

20 mg of each catalyst was suspended in 100 mL of methyl orange (MO) aqueous solution ( $5.0 \times 10^{-5}$  M), and then the suspension was placed in quartz tube and stirred for overnight in the absence of light to obtain the equilibrium adsorption on the catalyst surface. UV irradiation was carried out using a 2  $\times$  4 W fluorescent Hg-lamp (Philips TUV 4 W, the strongest emission at 254 nm). After a given irradiation time, about 5 mL of the mixture was withdrawn, and the catalysts were separated from the suspensions by centrifugation. The photocatalytic degradation process was monitored by a UV–vis spectrophotometer (Lambda 950) by measuring the absorption of MO at 464 nm.

## 3. Results and discussion

### 3.1. Formation of Sn<sub>1-x</sub>Zn<sub>x</sub>O<sub>2-x</sub> and ZnO/Sn<sub>1-x</sub>Zn<sub>x</sub>O<sub>2-x</sub> heterojunction



In the first solvothermal process, both Sn<sup>4+</sup> and Zn<sup>2+</sup> could be hydrolyzed and the product SnO<sub>2</sub> (or Sn<sub>1-x</sub>Zn<sub>x</sub>O<sub>2-x</sub>) is stable even at low pH conditions, while ZnO is easily dissolved [1]. Zn<sup>2+</sup> and Sn<sup>4+</sup> precursors with the Zn/Sn ratio of 2:1 were used with no additional alkali being involved; therefore, the formation of Zn<sup>2+</sup> doped SnO<sub>2</sub> can proceed as Eqs. (1) and (2), since Zn<sup>2+</sup> and Sn<sup>4+</sup> have close ionic radii (74 pm vs 69 pm). In this step, Sn<sup>4+</sup> and Zn<sup>2+</sup> are hydrolyzed by traces of chemically combined water originated from the raw materials to form complex Sn<sub>1-x</sub>Zn<sub>x</sub>(OH)<sub>4-2x</sub> (Eq. (1)). The release of H<sup>+</sup> was confirmed by the low pH value of 1.2 measured after the reaction. In the next solvothermal process, when NaOH ethanol solution was added, Zn(OH)<sub>4</sub><sup>2-</sup> was formed, and the intermolecular dehydrolysis led to the heterointerface between Sn<sub>1-x</sub>Zn<sub>x</sub>O<sub>2-x</sub>

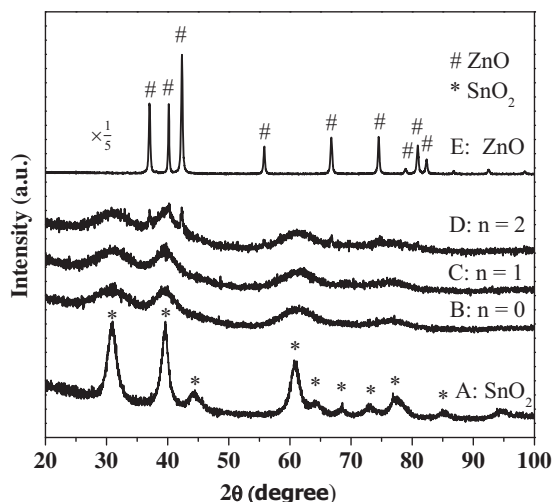


**Fig. 1.** XRD patterns of sample A:  $\text{SnO}_2$ , samples B–D prepared using 2n mL of NaOH ethanol solution (B:  $n = 0$ ; C:  $n = 1$ ; and D:  $n = 2$ ), and E: ZnO.

and ZnO, the reactions for the formation of  $\text{ZnO}/\text{Sn}_{1-x}\text{Zn}_x\text{O}_{2-x}$  heterostructure can be formulated as Eqs. (3) and (4).

### 3.2. XRD analysis

The XRD patterns of the as-prepared samples are shown in Fig. 1. All diffraction peaks in Fig. 1A and E are in good agreement with those of standard patterns for tetragonal rutile  $\text{SnO}_2$  (JCPDS file no. 41-1445) and hexagonal wurtzite ZnO (JCPDS file no. 36-1451), respectively. The diffraction peaks marked with “#” and “\*” are indexed to hexagonal wurtzite ZnO and tetragonal rutile  $\text{SnO}_2$ , respectively. The diffraction peaks of both samples A and E are sharp and intense, revealing the highly crystalline character of pure  $\text{SnO}_2$  and ZnO. Samples B–D mainly show  $\text{SnO}_2$  pattern. Comparing FWHM of the  $\text{SnO}_2$  peaks in samples B–D with those in the pure  $\text{SnO}_2$ , the diffraction peaks in samples B–D are much broader and weaker than those in pure  $\text{SnO}_2$ . This indicates that  $\text{Zn}^{2+}$  injection leads to semicrystalline products or small crystallites of the samples [32,34]. In Fig. 1D, there are two sets of diffraction peaks for sample D, indicating that the sample is composite materials containing  $\text{SnO}_2$  and ZnO. All diffraction peaks in sample B and C are the same as those in sample A (pure  $\text{SnO}_2$ ), indicating that they might be  $\text{SnO}_2$ ,  $\text{Sn}_{1-x}\text{Zn}_x\text{O}_{2-x}$  or  $\text{ZnO}/\text{Sn}_{1-x}\text{Zn}_x\text{O}_{2-x}$  with highly dispersed ZnO nanocrystals (suppose that the small amount of highly dispersed ZnO nanocrystals exist under the detect limitation of XRD). X-ray fluorescence (XRF) spectroscopy showed that sample B may be  $\text{Sn}_{1-x}\text{Zn}_x\text{O}_{2-x}$  with the  $\text{Zn}/(\text{Zn} + \text{Sn})$  molar ratio of 9%, since ZnO cannot be formed in this acidic solution (pH 1.2). NaOH was used for sample D preparation, and about 38 mol% of Zn element and 62 mol% of Sn element were detected by XRF. Therefore, the composition of sample D may be  $\text{ZnO}/\text{Sn}_{1-x}\text{Zn}_x\text{O}_{2-x}$ . These results can be further confirmed by FTIR and Raman analyses discussed later.

### 3.3. UV–vis diffuse reflectance spectra (DRS)

Diffuse reflectance spectroscopy (DRS) is used to study the optical absorption of materials. Fig. 2 shows the UV–vis diffuse reflectance spectra of as-prepared samples. The absorption edges of the as-synthesized pure  $\text{SnO}_2$  and ZnO are located at about 330 and 380 nm, respectively, corresponding to their distinct interband transitions. The absorption edges for samples B–D are located around 300 nm. Among them, sample C has slightly larger band gap than samples B and D, indicating a little higher redox capacity, which can contribute to its photocatalytic activity. Sample D

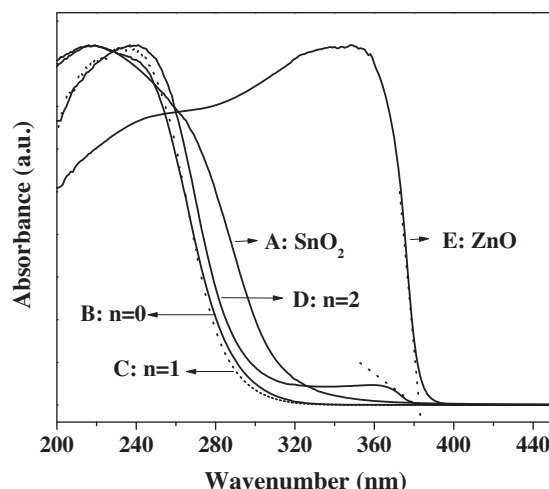


**Fig. 2.** UV–vis diffuse-reflectance spectra of sample A:  $\text{SnO}_2$ , samples B–D prepared using 2n mL of NaOH ethanol solution (B:  $n = 0$ ; C:  $n = 1$ , and D:  $n = 2$ ), and E: ZnO.

gives two absorption edges about 305 nm and 380 nm, which are expected for the interband transitions of  $\text{SnO}_2$  and ZnO, respectively. The  $\text{SnO}_2$  absorption edges in samples B–D are blue-shifted to about 300 nm, compared to that (330 nm) in sample A, pure  $\text{SnO}_2$ . Such shift may be attributed to the decrease of crystal size, resulting from Zn doping.

### 3.4. Fourier transform infrared spectroscopy (FTIR)

The chemical species absorbed on the sample surfaces were investigated by infrared spectra. The normal modes of vibrations at the Brillouin zone of  $\text{SnO}_2$  with a rutile structure and symmetry  $D_{4h}^{14}$  are given by [35]:

$$\Gamma = 1A_{1g} + 1A_{2g} + 1A_{2u} + 1B_{1g} + 1B_{2g} + 2B_{1u} + 1E_g + 3E_u. \quad (5)$$

Among these,  $A_{1g}$ ,  $B_{1g}$ ,  $B_{2g}$ , and  $E_g$  are Raman active modes, and  $A_{2u}$  and  $E_u$  are IR active modes. In Fig. 3, compared to pure ZnO and  $\text{SnO}_2$ , the samples B–D containing Zn doped  $\text{SnO}_2$  show much sharper band at  $1616 \text{ cm}^{-1}$  correspond to the bending vibrations of  $-\text{OH}$  group in water. The richness of surface  $-\text{OH}$  group is usually beneficial to photocatalytic activity. Two bands at 654 and  $518 \text{ cm}^{-1}$  are characteristic of the intrinsic vibrations for pure  $\text{SnO}_2$

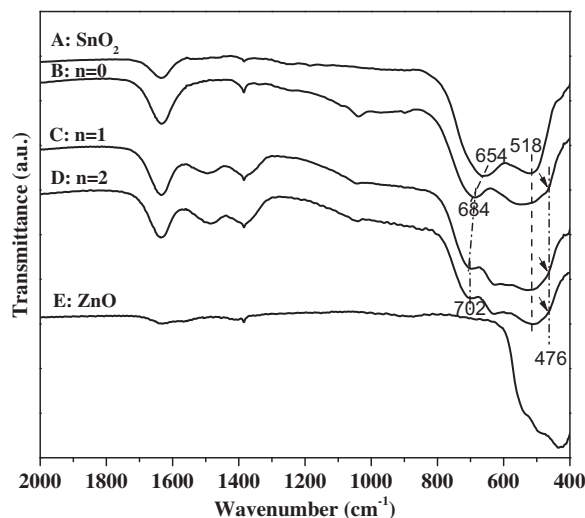


**Fig. 3.** IR spectra of sample A:  $\text{SnO}_2$ , samples B–D prepared using 2n mL of NaOH ethanol solution (B:  $n = 0$ ; C:  $n = 1$ ; and D:  $n = 2$ ), and E: ZnO.

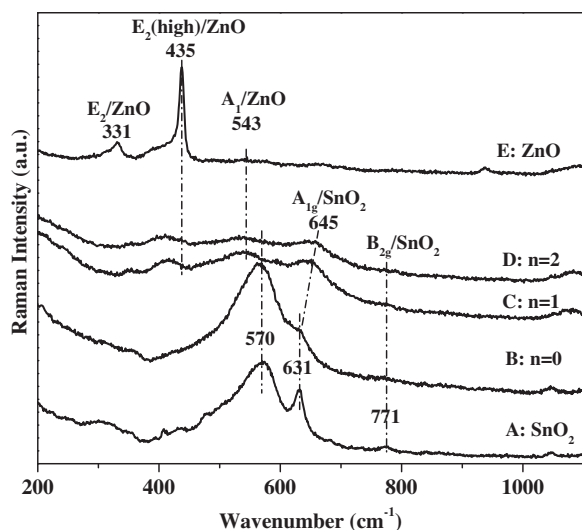


**Fig. 4.** The Raman spectra of sample A:  $\text{SnO}_2$ , samples B–D prepared using 2n mL of NaOH ethanol solution (B:  $n=0$ ; C:  $n=1$ ; and D:  $n=2$ ), and E: ZnO.

(sample A) [32]. The band observed at  $654\text{ cm}^{-1}$  is attributed to the  $E_u$  mode of anti-symmetric Sn–O stretching vibration, while the one at  $518\text{ cm}^{-1}$  is assigned to the vibration of the Sn–OH terminal bonds on the surface of  $\text{SnO}_2$  nanocrystals [36]. It is interesting to note that  $\text{Zn}^{2+}$  doping in  $\text{SnO}_2$  nanocrystals leads to a  $30\text{ cm}^{-1}$  shift of the  $E_u$  mode toward higher wavenumber from  $654\text{ cm}^{-1}$  for pure  $\text{SnO}_2$  to  $684\text{ cm}^{-1}$  for  $\text{Sn}_{1-x}\text{Zn}_x\text{O}_{2-x}$ , and then to  $702\text{ cm}^{-1}$  for samples C and D ( $\text{ZnO}/\text{Sn}_{1-x}\text{Zn}_x\text{O}_{2-x}$ ). A blue-shift of the  $E_u$  mode was observed when the particle size of  $\text{SnO}_2$  reduced [32,37]. Therefore, the size decrease of  $\text{Sn}_{1-x}\text{Zn}_x\text{O}_{2-x}$  nanocatalysts from Zn doped  $\text{SnO}_2$  could contribute to the blue-shift of the  $E_u$  mode, which agrees with XRD and DRS results. Another possibility may lie in the substitution of  $\text{Zn}^{2+}$  for  $\text{Sn}^{4+}$  by doping. To explain these phenomena, the calculation of IR absorption band is simplified by a physical model – harmonic oscillator. The wavenumber ( $\sigma$ ) and vibration energy ( $\Delta E_v$ ) are expressed as follows [38]:

$$\sigma = \frac{1}{2\pi c} \sqrt{\frac{k}{\mu}} \quad (\text{cm}^{-1}) \quad (6)$$

$$\Delta E_v = \frac{h}{2\pi} \sqrt{\frac{k}{\mu}} \quad (\text{eV}) \quad (7)$$

where  $c$ ,  $k$ ,  $\mu$ , and  $h$  represent velocity of light, bond force constant, reduced mass, and Planck constant, respectively. Based on these equations, the substitution of  $\text{Zn}^{2+}$  for  $\text{Sn}^{4+}$  leads to the increase of wavenumber ( $\sigma$ ), as  $\mu(\text{Zn})$  is smaller than  $\mu(\text{Sn})$ . Therefore, Zn doping should be responsible for the shift of  $E_u$  mode of  $\text{SnO}_2$ . In addition, another new mode at  $476\text{ cm}^{-1}$  (indicated by arrows) was observed in samples B–D, and it can be assigned to the Sn–O–Zn band, which further confirms the formation of  $\text{Sn}_{1-x}\text{Zn}_x\text{O}_{2-x}$  [32]. The similarity of the infrared spectra for samples C and D indicates that they may have the same chemical species,  $\text{ZnO}/\text{Sn}_{1-x}\text{Zn}_x\text{O}_{2-x}$ .

### 3.5. Raman scattering

The crystal structures and size effects of samples A–E were also investigated by Raman spectroscopy, as shown in Fig. 4. The tetragonal rutile  $\text{SnO}_2$  belongs to the  $D_{4h}^{14}$  space group with the optical modes  $A_{1g}$ ,  $B_{1g}$ ,  $B_{2g}$  and  $E_g$  [16,35]. In sample A (pure  $\text{SnO}_2$ ), the band around  $570\text{ cm}^{-1}$  is ascribed to Sn–O stretching mode [35], and the peaks centered at  $631$  and  $771\text{ cm}^{-1}$  can be assigned to the  $A_{1g}$  and  $B_{2g}$  modes of  $\text{SnO}_2$ , respectively, which are related to the

expansion and contraction vibration modes of Sn–O bonds in the rutile structure of  $\text{SnO}_2$  [16]. The  $B_{2g}$  mode in samples B–D disappeared, due to very small  $\text{SnO}_2$  nanoparticles after doping Zn [39], which agrees with the results from XRD and DRS. Compared with sample A, the peak at  $631\text{ cm}^{-1}$  of sample B becomes weaker and broader. It has been reported that the weakness and broadening of  $A_{1g}$ , Sn–O symmetric stretching band resulted from doping [35]. Therefore, this can be attributed to  $\text{Zn}^{2+}$  doping in  $\text{SnO}_2$  and the formation of  $\text{Sn}_{1-x}\text{Zn}_x\text{O}_{2-x}$  solid solution. For samples C and D, the formation of  $\text{ZnO}/\text{Sn}_{1-x}\text{Zn}_x\text{O}_{2-x}$  heterostructure probably leads to a successive shift of this peak toward higher wavenumber from  $631\text{ cm}^{-1}$  to  $645\text{ cm}^{-1}$ .

ZnO with a wurtzite-type structure belongs to the  $C_{6v}$  space group or 6mm symmetry with the photon modes  $E_2$  (high),  $A_1$  (TO-transversal acoustic mode and LO longitudinal optical components) and  $E_1$  (TO and LO) [16,40–42]. In sample E (pure ZnO), the peaks centered at  $331$ ,  $435$ , and  $543\text{ cm}^{-1}$  can be attributed to the second order  $E_2$ , high frequency  $E_2$  (high), and second order  $A_1$  modes of ZnO, respectively [42]. The high intensity and narrow width of  $E_2$  (high) peak indicates the good crystal quality of pure ZnO prepared.  $E_2$  (high) and second order  $A_1$  modes of ZnO appear very weak and broad in the spectra of samples C and D, indicating ZnO with small size or low crystallinity might be contained in samples C and D. This may correlate with the formation of highly dispersed ZnO on  $\text{Sn}_{1-x}\text{Zn}_x\text{O}_{2-x}$ .

### 3.6. X-ray photoemission spectroscopy (XPS)

X-ray photoelectron spectroscopy (XPS) is a very powerful tool for the experimental determination of heterojunction. To confirm the formation of heterojunction between ZnO and  $\text{Sn}_{1-x}\text{Zn}_x\text{O}_{2-x}$ , we conducted high-resolution XPS measurements of Zn and/or Sn species on  $\text{Sn}_{1-x}\text{Zn}_x\text{O}_{2-x}$  (sample B),  $\text{ZnO}/\text{Sn}_{1-x}\text{Zn}_x\text{O}_{2-x}$  (sample C) and ZnO (sample E). Fig. 5 displays the XPS spectra of the Zn 2p and Sn 3d core levels from samples B, C and E. Interestingly, for sample C, the Zn 2p peaks shift  $1.2\text{ eV}$  toward higher binding energy compared with sample E (Fig. 5a), whereas the Sn 3d core levels shift  $0.3\text{ eV}$  toward lower binding energy compared with sample B (Fig. 5b). The shift of Zn 2p and Sn 3d core levels toward to opposite directions is ascribed to the charge build-up at the interface between ZnO and  $\text{Sn}_{1-x}\text{Zn}_x\text{O}_{2-x}$  due to the formation of  $\text{ZnO}/\text{Sn}_{1-x}\text{Zn}_x\text{O}_{2-x}$  heterojunction [43]. This phenomenon was also observed in II–VI/ $\text{Zn}_3\text{P}_2$  heterojunctions by the group of Atwater [44].

### 3.7. Brunauer–Emmett–Teller (BET) $N_2$ physisorption

The texture of the as-synthesized samples was characterized by  $N_2$  physisorption experiments, as shown in Fig. 6. It can be clearly seen in Fig. 6a that sample A presents typical type III isotherm with a distinct H3 hysteresis loop according to the IUPAC classification, while the samples B–D containing  $\text{Sn}_{1-x}\text{Zn}_x\text{O}_{2-x}$  exhibit representative type IV isotherms with a distinct H2 hysteresis loop in the range of  $0.4\text{--}1.0\text{ }P/P_0$ , which shows mesoporous characteristic [45]. The corresponding pore size distributions (Fig. 6b) of the as-synthesized samples, calculated from desorption branches of the  $N_2$  isotherms by the BJH method, show that a pore size distribution is centered between  $3\text{--}4\text{ nm}$  for samples B–D, and the porous nature of sample A can be neglected. One can see that samples B–D exhibit much higher pore volumes and BET specific surface areas than sample A, pure  $\text{SnO}_2$ . The order of the BET specific surface areas of the as-synthesized samples is  $S_B$  ( $n=0$ ,  $S_{\text{BET}} = 322.7\text{ m}^2/\text{g}$ )  $>$   $S_C$  ( $n=1$ ,  $S_{\text{BET}} = 262.8\text{ m}^2/\text{g}$ )  $>$   $S_D$  ( $n=2$ ,  $S_{\text{BET}} = 232.2\text{ m}^2/\text{g}$ )  $\gg$   $S_A$  ( $\text{SnO}_2$ ,  $S_{\text{BET}} = 89.3\text{ m}^2/\text{g}$ ). When  $\text{Zn}^{2+}$  was introduced into  $\text{SnCl}_4$  ethanol solution without NaOH, uniformly structured mesopores in  $\text{Sn}_{1-x}\text{Zn}_x\text{O}_{2-x}$  was obtained (sample B),



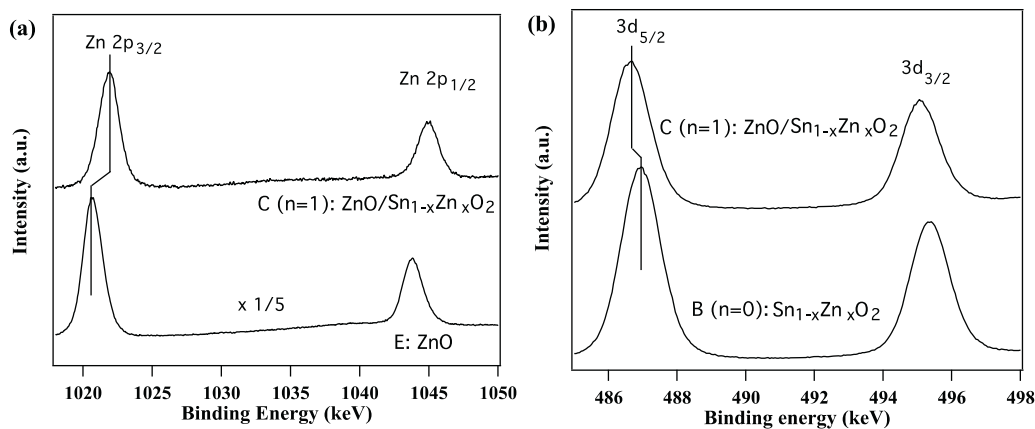


Fig. 5. High-resolution XPS spectra of (a) Zn 2p and (b) Sn 3d core levels measured on  $\text{Sn}_{1-x}\text{Zn}_x\text{O}_{2-x}$  (sample B),  $\text{ZnO}/\text{Sn}_{1-x}\text{Zn}_x\text{O}_{2-x}$  (sample C) and ZnO (sample E).

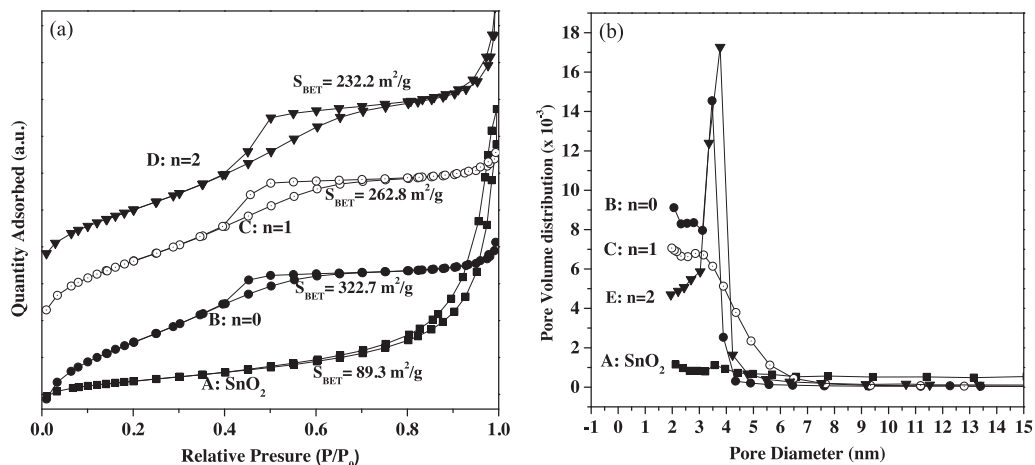


Fig. 6. (a) Nitrogen adsorption–desorption isotherm and (b) pore size distribution of sample A:  $\text{SnO}_2$ , samples B–D prepared using 2n mL of NaOH ethanol solution (B:  $n=0$ ; C:  $n=1$ ; and D:  $n=2$ ).

and the formation of mesoporous  $\text{Sn}_{1-x}\text{Zn}_x\text{O}_{2-x}$  leads to dramatic increase of surface area. By contrary, the appearance of  $\text{ZnO}/\text{Sn}_{1-x}\text{Zn}_x\text{O}_{2-x}$  has an opposite effect on the specific surface area in samples C and D. The larger surface areas for samples B–D can benefit to photocatalytic activity, which will be described later.

### 3.8. Analysis of hydroxyl radicals ( $\cdot\text{OH}$ )

It is assumed that photo-induced holes react with hydroxide ions or water absorbed on the surface to produce highly oxidizing  $\cdot\text{OH}$  radicals, which are often considered to be the major species responsible for the photocatalytic oxidation [33]. The formation of hydroxyl radicals ( $\cdot\text{OH}$ ) on the surface of UV-illuminated photocatalysts can be detected by a photoluminescence (PL) technique with coumarin as a probe molecule [33]. Coumarin readily reacts with  $\cdot\text{OH}$  to produce highly fluorescent product, 7-hydroxycoumarin. The intensity of the PL peak of 7-hydroxycoumarin is proportional to the amount of  $\cdot\text{OH}$  radicals produced in water. Fig. 7a shows the  $\cdot\text{OH}$  trapping photoluminescence spectra of sample C ( $n=1$ ) in a coumarin solution under UV-light irradiation. The observed peaks indicate that fluorescent product, 7-hydroxycoumarin was continuously formed from the specific reaction between  $\cdot\text{OH}$  and coumarin along with the UV irradiation. Fig. 7b shows the fluorescent intensity of 7-hydroxycoumarin at 460 nm as a function of irradiation time. An induction period for samples B–D is observed in the first 5 min of UV light irradiation. The induction period could be ascribed to the

strong absorption of 7-hydroxycoumarin on their surface and/or the gradual release of 7-hydroxycoumarin from their surface, resulting from their high surface area. As shown in Fig. 7b, sample C exhibits the fastest formation of  $\cdot\text{OH}$  radical, indicating the highest separation efficiency of electron–hole pairs in this sample.

### 3.9. Photocatalytic activity

Photocatalytic degradation of MO under UV-irradiation was performed by the as-synthesized samples B–D, in comparison with highly photoactive commercial  $\text{TiO}_2$  (Degussa P-25), the mixture of ZnO and  $\text{Sn}_{1-x}\text{Zn}_x\text{O}_{2-x}$ , pure ZnO and  $\text{SnO}_2$ . Temporal changes in the concentration of MO were monitored with UV-vis spectroscopy by the absorption at 464 nm. Fig. 8 shows the kinetics of MO photocatalytic degradation without and with different photocatalysts.  $C_0$  and  $C$  are the equilibrium concentrations of MO before and after UV irradiation, respectively. No degradation can be observed without catalyst or without irradiation. The degradation of MO followed apparent 0–1 order kinetics, depending on the sample used. Highly efficient degradation (e.g. by samples B–D) showed pseudo first-order kinetics, while pseudo zero-order kinetics was observed in slow degradation (e.g. by sample A). As we know, ultrafine photocatalyst powders normally exhibit high photocatalytic activity because of their small particle size with high surface area, which can shorten the transfer distance of photo-generated charge carriers to the catalyst surface, and increase the number of active surface sites where the charge carriers react

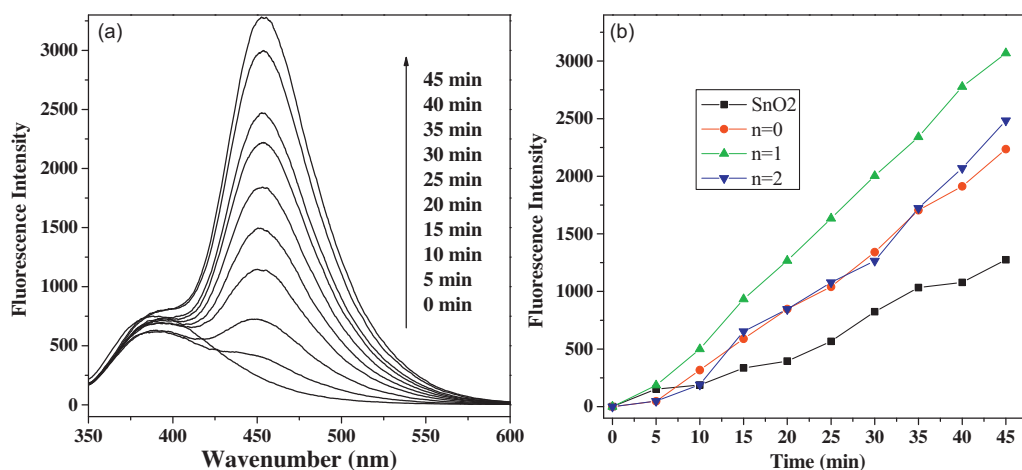


**Fig. 7.** (a) PL spectra of 7-hydroxycoumarin observed during UV irradiation of sample C in coumarin solution at room temperature. 10 mg of catalyst was added to 100 mL of  $1 \times 10^{-3}$  M coumarin solution in a 200 mL Pyrex glass vessel. Each fluorescence spectrum was recorded at every 5 min interval, under the excitation with the wavelength of 332 nm. (b) Plot of the fluorescence intensity at 460 nm against irradiation time in the presence of sample A  $\text{SnO}_2$ , samples B–D prepared using 2n mL of NaOH ethanol solution (B:  $n=0$ ; C:  $n=1$ ; and D:  $n=2$ ).

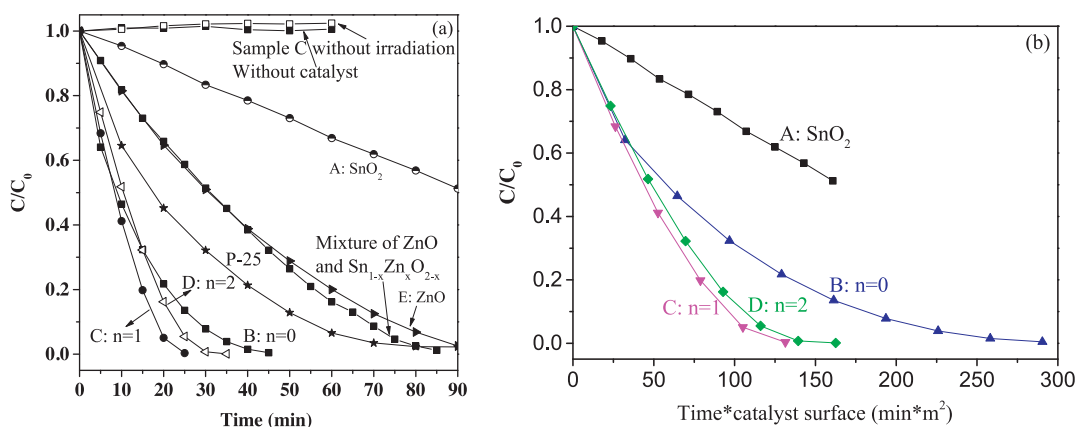


**Fig. 8.** (a) Photodegradation of MO by the as-synthesized sample A:  $\text{SnO}_2$ , samples B–D prepared using 2n mL of NaOH ethanol solution (B:  $n=0$ ; C:  $n=1$ ; and D:  $n=2$ ), and E: ZnO. The commercial  $\text{TiO}_2$  (Degussa P-25), the mixture of ZnO and  $\text{Sn}_{1-x}\text{Zn}_x\text{O}_{2-x}$ , and pure ZnO and  $\text{SnO}_2$  were used as references. (b) Normalized degradation curves for some samples by taking their specific surface areas into account. Catalyst amount used in all experiments is 20 mg. The physical meaning of this figure is to show the reaction process per unit of time and surface area.

with absorbed molecules to form hydroxyl and superoxide radicals. Therefore, samples B–D shows much higher photocatalytic activity than pure ZnO,  $\text{SnO}_2$ , and even P-25. It was reported that  $\text{Zn}^{2+}$  doping can enhance the photocatalytic activity due to prohibiting the coalescence of tiny  $\text{SnO}_2$  crystals to larger particles [32]. Interestingly, we find that the highest photocatalytic activities are obtained by samples C and D, although their specific surface areas are lower than sample B (see Fig. 6a). When the degradation curves are normalized to the specific surface areas of samples B–D, the superiority in the intrinsic photoactivity of samples C and D to sample B is even more apparent (Fig. 8b). It is well known that the fast recombination of the photogenerated electron–hole pairs decreases the photon efficiency. The  $\text{ZnO}/\text{Sn}_{1-x}\text{Zn}_x\text{O}_{2-x}$  heterostructure in samples C and D can facilitate photocatalytic degradation of MO by promoting the charge separation. We assume Zn doped  $\text{SnO}_2$  ( $\text{Sn}_{1-x}\text{Zn}_x\text{O}_{2-x}$ ) has the similar band positions as pure  $\text{SnO}_2$ . When the  $\text{ZnO}/\text{Sn}_{1-x}\text{Zn}_x\text{O}_{2-x}$  catalyst is irradiated by UV light with photon energy higher than the band gaps of  $\text{Sn}_{1-x}\text{Zn}_x\text{O}_{2-x}$  and ZnO, the photogenerated electrons and holes are separated by electrons moving to the  $\text{Sn}_{1-x}\text{Zn}_x\text{O}_{2-x}$  side and holes to the ZnO side [26,29]. Therefore, photocatalytic activities of samples C and D are excessively compensated by the

formation of heterojunction  $\text{ZnO}/\text{Sn}_{1-x}\text{Zn}_x\text{O}_{2-x}$ , although their specific surface areas decrease from  $\text{Sn}_{1-x}\text{Zn}_x\text{O}_{2-x}$  (sample B). The heterojunction does not exist in the mechanical mixture of ZnO and  $\text{Sn}_{1-x}\text{Zn}_x\text{O}_{2-x}$ , which only showed the photocatalytic activity between those of ZnO and  $\text{Sn}_{1-x}\text{Zn}_x\text{O}_{2-x}$  (Fig. 8a).

#### 4. Conclusion

A novel configuration of porous  $\text{ZnO}/\text{Sn}_{1-x}\text{Zn}_x\text{O}_{2-x}$  heterostructured nanocatalysts with high photocatalytic activity was obtained through a simple two-step solvothermal method. Zn doping in  $\text{SnO}_2$  shows a significant influence on prohibiting the coalescence of  $\text{SnO}_2$  crystals to large particles, leading to high specific surface area and large band gap, which is normally in favor of photocatalytic activity. The formation of  $\text{ZnO}/\text{Sn}_{1-x}\text{Zn}_x\text{O}_{2-x}$  heterostructure improves the separation of photogenerated electron–hole pairs due to the potential difference between  $\text{Sn}_{1-x}\text{Zn}_x\text{O}_{2-x}$  and ZnO, which also facilitates photocatalytic reaction. Taken together, these results provide further insight into the synergistic effects of metal ion doping and semiconductor/semiconductor heterojunction on photocatalytic activity enhancement.

## Acknowledgements

The authors acknowledge the financial support from Department of Science of the People's Republic of China (20771025), Department of Science & Technology of Fujian Province (2005H201-2), Ångpanneföreningen's Foundation for Research and Development, and Environmental Foundation from the Swedish Association of Graduate Engineers.

## References

- [1] L. Zhang, H. Cheng, R. Zong, Y. Zhu, *Journal of Physical Chemistry C* 113 (2009) 2368–2374.
- [2] A. Fujishima, K. Honda, *Nature* 238 (1972) 37–38.
- [3] M. Gratzel, *Nature* 414 (2001) 338–344.
- [4] J. Zhu, M. Zäch, *Current Opinion in Colloid & Interface Science* 14 (2009) 260–269.
- [5] J. Zhu, D. Chakarov, M. Zäch, in: L. Zang (Ed.), *Energy Efficiency and Renewable Energy Through Nanotechnology*, Springer, London, 2011, pp. 441–486.
- [6] J. Zhu, in: R. Meyers (Ed.), *Encyclopedia of Sustainability Science and Technology*, Springer, New York, 2012, pp. 7881–7901.
- [7] M.R. Hoffmann, S.T. Martin, W. Choi, D.W. Bahnemann, *Chemical Reviews* 95 (1995) 69–96.
- [8] R. Wang, K. Hashimoto, A. Fujishima, M. Chikuni, E. Kojima, A. Kitamura, M. Shimohigoshi, T. Watanabe, *Nature* 388 (1997) 431–432.
- [9] H. Fu, T. Xu, S. Zhu, Y. Zhu, *Environmental Science & Technology* 42 (2008) 8064–8069.
- [10] Q. Xiao, Z. Si, J. Zhang, C. Xiao, X. Tan, *Journal of Hazardous Materials* 150 (2008) 62–67.
- [11] W.Y. Choi, A. Termin, M.R. Hoffmann, *Journal of Physical Chemistry* 98 (1994) 13669–13679.
- [12] M. Anpo, M. Takeuchi, K. Ikeue, S. Dohshi, *Current Opinion in Solid State & Materials Science* 6 (2002) 381–388.
- [13] T. Kamegawa, J. Sonoda, K. Sugimura, K. Mori, H. Yamashita, *Journal of Alloys and Compounds* 486 (2009) 685–688.
- [14] Z. Liu, D.D. Sun, P. Guo, J.O. Leckie, *Nano Letters* 7 (2006) 1081–1085.
- [15] W.W. Wang, Y.J. Zhu, L.X. Yang, *Advanced Functional Materials* 17 (2007) 59–64.
- [16] E.M. Seftel, E. Popovici, M. Mertens, E.A. Stefaniak, R. Van Grieken, P. Cool, E.F. Vansant, *Applied Catalysis B: Environmental* 84 (2008) 699–705.
- [17] C. Li, T. Ahmed, M. Ma, T. Edvinsson, J. Zhu, *Applied Catalysis B: Environmental* 138–139 (2013) 175–183.
- [18] M.J. Height, S.E. Pratsinis, O. Mekasuwandumrong, P. Praserthdam, *Applied Catalysis B: Environmental* 63 (2006) 305–312.
- [19] J.-J. Wu, C.-H. Tseng, *Applied Catalysis B: Environmental* 66 (2006) 51–57.
- [20] Y. Zheng, L. Zheng, Y. Zhan, X. Lin, Q. Zheng, K. Wei, *Inorganic Chemistry* 46 (2007) 6980–6986.
- [21] Y. Zheng, C. Chen, Y. Zhan, X. Lin, Q. Zheng, K. Wei, J. Zhu, *Journal of Physical Chemistry C* 112 (2008) 10773–10777.
- [22] C.G. Silva, R. Juarez, T. Marino, R. Molinari, H. Garcia, *Journal of the American Chemical Society* 133 (2011) 595–602.
- [23] A. Primo, T. Marino, A. Corma, R. Molinari, H. Garcia, *Journal of the American Chemical Society* 133 (2011) 6930–6933.
- [24] K. Fuku, T. Kamegawa, K. Mori, H. Yamashita, *Chemistry – An Asian Journal* 7 (2012) 1366–1371.
- [25] Q. Kuang, Z.-Y. Jiang, Z.-X. Xie, S.-C. Lin, Z.-W. Lin, S.-Y. Xie, R.-B. Huang, L.-S. Zheng, *Journal of the American Chemical Society* 127 (2005) 11777–11784.
- [26] M.T. Uddin, Y. Nicolas, C. Olivier, T. Toupance, L. Servant, M.M. Müller, H.-J. Kleebe, J. Ziegler, W. Jaegermann, *Inorganic Chemistry* 51 (2012) 7764–7773.
- [27] L.R. Zheng, Y.H. Zheng, C.Q. Chen, Y.Y. Zhan, X.Y. Lin, Q. Zheng, K.M. Wei, J.F. Zhu, *Inorganic Chemistry* 48 (2009) 1819–1825.
- [28] L.R. Zheng, Y.H. Zheng, C.Q. Chen, Y.Y. Zhan, X.Y. Lin, Q. Zheng, K.M. Wei, *ChemPlusChem* 77 (2012) 217–223.
- [29] L. Zheng, Y. Zheng, C. Chen, Y. Zhan, X. Lin, Q. Zheng, K. Wei, J. Zhu, *Inorganic Chemistry* 48 (2009) 1819–1825.
- [30] H.T. Huang, S.Q. Tian, J. Xu, Z. Xie, D.W. Zeng, D. Chen, G.Z. Shen, *Nanotechnology* 23 (2012) 105502.
- [31] T. Jia, W.M. Wang, F. Long, Z.Y. Fu, H. Wang, Q.J. Zhang, *Journal of Physical Chemistry C* 113 (2009) 9071–9077.
- [32] L. Li, J. Liu, Y. Su, G. Li, X. Chen, X. Qiu, T. Yan, *Nanotechnology* 20 (2009) 155706.
- [33] K.-i. Ishibashi, A. Fujishima, T. Watanabe, K. Hashimoto, *Electrochemistry Communications* 2 (2000) 207–210.
- [34] H.P. Klug, L.E. Alexander, *X-Ray Diffraction Procedures: For Polycrystalline and Amorphous Materials*, Wiley, New York, 1974.
- [35] X. Mathew, J.P. Enriquez, C. Mejia-Garcia, G. Contreras-Puente, M.A. Cortes-Jacome, J.A.T. Antonio, J. Hays, A. Punnoose, *Journal of Applied Physics* 100 (2006).
- [36] F. Gu, S. Fen Wang, C. Feng Song, M. Kai Lü, Y. Xin Qi, G. Jun Zhou, D. Xu, D. Rong Yuan, *Chemical Physics Letters* 372 (2003) 451–454.
- [37] B. Yu, L. Guo, Z. Yang, C. Zhu, F. Gan, G. Zhang, G. Tang, X. Wu, W. Chen, *Physics Letters A* 251 (1999) 67–72.
- [38] W.O. George, P.S. McIntyre, D.J. Mowthorpe, *ACOL, Infrared Spectroscopy*, Published on behalf of ACOL, London by Wiley, 1987.
- [39] P.L. Johnson, D. Teeters, *Solid State Ionics* 177 (2006) 2821–2825.
- [40] J.M. Calleja, M. Cardona, *Physical Review B* 16 (1977) 3753–3761.
- [41] O. Lupan, L. Chow, G. Chai, B. Roldan, A. Naitabdi, A. Schulte, H. Heinrich, *Materials Science and Engineering: B* 145 (2007) 57–66.
- [42] R. Cuscó, E. Alarcón-Lladó, J. Ibáñez, L. Artús, J. Jiménez, B. Wang, M.J. Callahan, *Physical Review B* 75 (2007) 165202.
- [43] M. Perego, G. Seguíni, *Journal of Applied Physics* 110 (2011) 053711.
- [44] J.P. Bosco, D.O. Scanlon, G.W. Watson, N.S. Lewis, H.A. Atwater, *Journal of Applied Physics* 113 (2013) 203705.
- [45] K.S.W. Sing, D.H. Everett, R.A.W. Haul, L. Moscou, R.A. Pierotti, J. Rouquerol, T. Siemieniowska, *Pure and Applied Chemistry* 57 (1985) 603–619.